Probing Proximity-Induced Superconductivity in InAs Nanowires Using Built-In Barriers

Tosson Elalaily[1,2] Olivér Kürtössy,[1] Valentina Zannier,[3] Zoltán Scherübl,[1] István Endre Lukács,[4] Pawan Srivastava,[1] Francesca Rossi,[5] Lucia Sorba,[3] Szabolcs Csonka,[1,*] and Péter Makk[1,†]

[1] *Department of Physics, Budapest University of Technology and Economics and Nanoelectronics 'Momentum' Research Group of the Hungarian Academy of Sciences, Budafoki ut 8, 1111 Budapest, Hungary*

[2] *Department of Physics, Faculty of Science, Tanta University, Al-Geish St., 31527 Tanta, Gharbia, Egypt*

[3] *NEST, Istituto Nanoscienze-CNR and Scuola Normale Superiore, Piazza San Silvestro 12, I-56127 Pisa, Italy*

[4] *Center for Energy Research, Institute of Technical Physics and Material Science, Konkoly-Thege Miklós út 29-33, H-1121 Budapest, Hungary*

[5] *IMEM-CNR, Parco Area delle Scienze 37/A, I-43124 Parma, Italy*

Bound states in superconductor-nanowire hybrid devices play a central role, carrying information on ground-state properties (Shiba or Andreev states) or on the topological properties of the system (Majorana states). The spectroscopy of such bound states relies on the formation of well-defined tunnel barriers, usually defined by gate electrodes, which results in smooth tunnel barriers. Here we used thin InP segments embedded into InAs nanowire during the growth process to form a sharp built-in tunnel barrier. Gate dependence and thermal-activation measurements are used to confirm the presence and estimate the height of this barrier. By coupling these wires to superconducting electrodes we investigate the gate-voltage dependence of the induced gap in the nanowire segment, which we can understand using a simple model based on Andreev bound states. Our results show that these built-in barriers are promising as future spectroscopic tools.

I. INTRODUCTION

Semiconducting nanowires [1] recently became one of the leading platforms for nanoscale hybrid devices. The reason for this lies in the high-quality materials available and also in the possibility to confine electrons using electrostatic gating. Therefore, these wires became a host for several fascinating systems: spin qubits [2], Andreev qubits [3,4], Cooper pair-splitter [5–8] devices, magnetic Weyl points, or the famous Majorana wires [9–12]. Particularly, InAs wires are very widely used due to large spin-orbit coupling, the simplicity of realizing electrical contacts, and the precise control of growth conditions that can be achieved. For most of these systems mentioned above, superconducting (SC) correlations are needed to be induced in the wires, which is achieved by coupling the wire to SC electrodes. This coupling results in proximity-induced superconductivity and the appearance of bound states in the wire. While these bound states can come in a different flavor from Andreev [3,4,13,14], Shiba [15–18] to

even Majorana states [9–12], their observation requires the formation of tunnel probes in the vicinity of these states.

Usually, to define tunnel barriers, electrostatic gates placed next to or below the wires are used [19,20]. While these gates allow some tunability of the coupling, the barriers formed are rather smooth and wide, due to the distance of the gate electrode from the wire and the finite width of the gate and wire. Moreover, such gates modify the potential profile in an extended region of the wire changing also the bound states that one wants to probe. However, well-defined sharp barriers can be formed by embedding InP segments into the InAs wire, during the growth procedure. The barrier originates from the different band alignment of the conduction band of InAs and InP, as shown in Fig. 1(b). Previous studies have shown that the barriers are atomically sharp, and their width can be controlled with the precision of a single atomic layer [21]. Using two of these barriers quantum dots were formed [22], which were used to study coupling asymmetries in a dot [23], the Stark effect [24–26], or thermal transport in quantum dots [27–29]. However, no studies have investigated how well these barriers can be used as a spectroscopy tool for superconducting bound states. Here we investigate the proximity effect in InAs wires using single InP segments

---

*szabolcs.csonka@mono.eik.bme.hu
†peter.makk@mail.bme.hu

as tunnel barriers [30]. We confirm the presence of the barriers using thermal-activation measurements. Coupling the wires to evaporated aluminium electrodes, superconducting proximity effect is induced in the InAs segment, which we probe with our detector. We find substantial conductance suppression at subgap voltages originating from the proximitized wire segment. These barriers are important for monitoring subgap states both in qubits or Majorana devices.

II. EXPERIMENTS

A. Device outline

We use InAs nanowires with very narrow InP segments grown with Au-assisted chemical beam epitaxy (CBE) [31]. The nanowires have a diameter of approximately 50 nm, with a narrow InP segment of thickness $a = 5.2 \pm 0.4$ nm. Figure 1(a) shows a TEM image of three InAs/InP nanowires where the InP segments are visible as a narrow dark region (also highlighted by the red rectangle). Previous studies using high-resolution TEM images have shown that the barriers are atomically sharp [21,28,30,32]. Due to the large difference between the energy gaps of InAs and InP (approximately 1 eV), the InP segment will act as a sharp potential barrier for the electrons in the conduction band of the InAs nanowire as illustrated in the schematic view of the band structure of an InAs/InP/InAs heterostructure in Fig. 1(b).
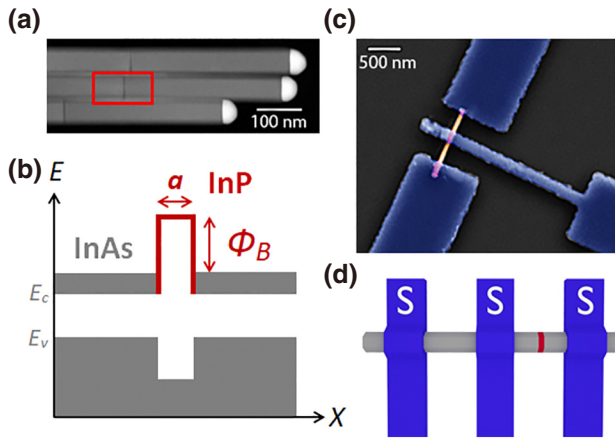

FIG. 1. Device structure. (a) TEM image of three InA nanowires deposited next to each other on a silicon substrate. The dark regions correspond to the InP segments (see red rectangle). (b) Schematic view of the bandstructure of an InAs/InP/InAs heterostructure. The conduction band of the InAs is slightly filled ($E_F > E_C$), however due to the larger bandgap of InP it acts as a tunnel barrier with height of Φ_B and width of a. A false-colored SEM image of the device is shown in (c) and a simplified schematic view is given in (d). The blue electrodes are superconducting aluminum (S). Two InAs segments are contacted by the electrodes, the right segment contains an InP barrier (red) and left one does not, which allows for comparative measurements.

To characterize the InP barriers, nanowires are deposited on silicon substrate with a 290-nm-thick oxide layer. Figure 1(c) shows a false-colored SEM image for a nanowire-based device with three superconductor aluminum electrodes (blue colored). Details of the fabrication are given in Sec. V. The device is fabricated such that the middle contact divides the nanowire into two segments: one of them contains the InP barrier, whereas the other section is a pure InAs segment for the purpose of comparative measurements [see Fig. 1(d)]. The length of the segments between the wire and the barrier is $L = 150$ nm, and the reference junction has the length of $2L$.

B. Thermal activation

The backgate response for the two segments has been investigated by using a standard lock-in technique. Figure 2(a) shows the measured conductance of the two segments as a function of backgate voltage at $T = 300$ K. Measurements at low temperature, $T = 4$ K, displaying similar features are shown in the Supplemental Material [33]. The gray line displays the conductance of the segment without the barrier, which shows a typical field-effect behavior of InAs nanowires with a pinchoff voltage close to $V_{BG} = -30$ V. Compared to this, the segment hosting the InP barrier has substantially reduced conductance (see red curve). While the conductance of a fully open nanowire exceeds $3\text{--}6G_0$ ($G_0 = 2e^2/h$), the conductance of the barrier segment is limited to $0.4\text{--}0.5G_0$. At large gate voltages the nanowire segments contain already several highly transmitting modes, therefore the reduction in this case can be attributed to the presence of the barrier.

To measure the effective height of this barrier, the *I-V* characteristic measurements are performed on the InP barrier segment at different temperatures as shown in Fig. 2(b). At higher temperatures electrons propagating in the InAs nanowire have sufficient energy to thermally go over the InP barrier, whereas at low temperatures the thermal activation is reduced. Using a simple model of a rectangular barrier the current I through the barrier as a function of temperature T is given by [30]

$$I = A_r A T^2 \exp\left[-e\varphi_B(V_{SD})/k_B T\right], \quad (1)$$

where T is the temperature, $\varphi_B(V_{SD})$ is the dc bias-dependent barrier height [see Fig. 2(b)], A is the nanowire cross-section area, A_r is Richardson constant and k_B and e are the Boltzmann constant and the electron charge, respectively. By plotting $\ln I/T^2$ vs $(1000/T)$ for the measured data as shown in Fig. 2(b) for six different positive and negative bias voltages, the effective barrier height at a given bias voltage can be estimated directly from the slope of the fitted lines.

The effective barrier height is calculated for bias voltages in the window of -0.2 to 0.2 V as shown in Fig. 2(d). A narrow window of ± 15 mV around zero bias is excluded
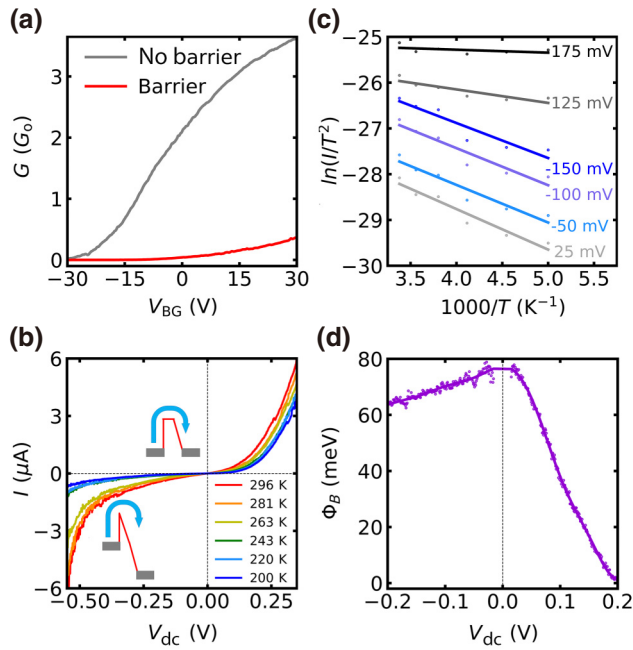
FIG. 2. Characterization of tunnel barriers. Panel (a) compares the conductance as a function backgate voltage for the segment with and without barrier at room temperature. The large decrease of conductance already at room temperature shows the presence of a barrier. Panel (b) shows I-V_{dc} curves measured at different temperatures through the segment containing the barrier. The conductance at low dc bias is reduced and increases rapidly at high bias as a hallmark of tunnel barrier. In (c), the curves of (b) are replotted as $\ln(I/T^2)$ vs approximately $1/T$ for different dc biases showing thermal-activation behavior. From the slope of the curves an effective barrier height can be extracted for different bias voltages, as shown in (d). The effective barrier height at zero bias corresponds to the barrier height.

from the analysis due to the small values of the current leading to large scattering on the effective barrier height. The estimated effective barrier height at zero bias is around 80 meV. One can also notice an asymmetry in the effective barrier height between positive and negative bias voltages. The lack of symmetry in bias voltage is already present in the I-V curves of (b), where the breakdown voltage is substantially different for forward and reverse bias. A possible reason for this might come from a structural asymmetry [34]: during the growth process the transition from InAs to InP is sharper than for the transition InP to InAs as shown by high-resolution TEM in Ref. [21] and illustrated by the insets of (b).

A second thing to notice is that the effective barrier height is smaller than expected from work-function arguments and also substantially smaller than measured in Refs. [30,32] with InP barrier thickness about 80 nm. The reason for this small value might come from the oversimplification of our model. First, the model uses a rectangular-shaped barrier, which might not be realistic for

such thin barriers, where the transition from InAs to InP is atomically sharp. The other one (InP-to-InAs) is slightly graded, and the transition is on a non-negligible length scale (about 5 nm). Moreover, the model neglects changes in the barrier shape due to the applied voltage and also neglects the effect of quantum tunneling, which are both relevant for such narrow barriers contrary to wide barriers studied before in Refs. [30,32,34].

C. Low-temperature superconducting spectroscopy

Superconducting spectroscopy using built-in barriers are performed in dilution refrigerator at a temperature of 30 mK. A small, 10 μV ac signal has been applied to the middle contact and the differential conductance in both segments is measured as a function of the backgate voltage V_{BG} and dc bias V_{SD}. Figures 3(a) and 3(b) show measurements on device segments without barrier and with barrier, respectively, and corresponding line cuts at
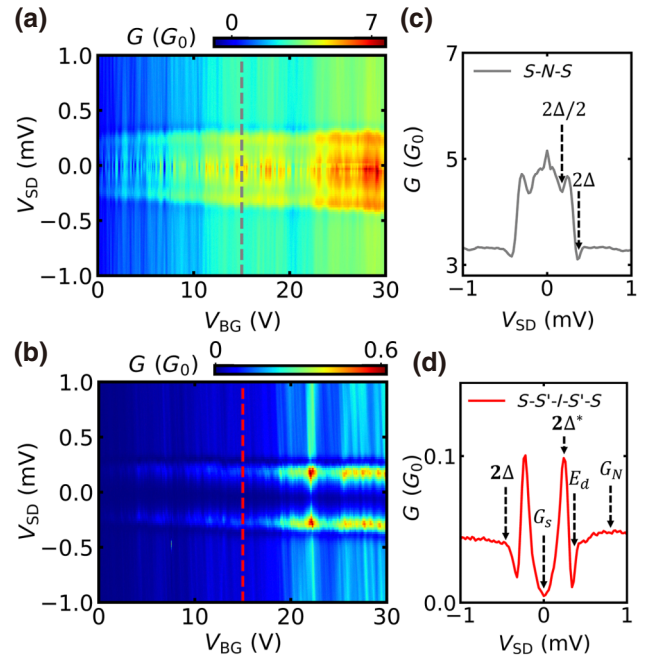

FIG. 3. Low-temperature superconductivity measurements. Differential conductance as a function of V_{SD} and V_{BG} for the InAs segment without barrier and with barrier shown in (a),(b), respectively. Corresponding cuts from (a),(b) at the positions of the dashed lines are shown on (c),(d), respectively. The structure without barrier on (c) shows a clear enhancement at low bias voltages and the presence of multiple Andreev reflection marked by arrows on (c). The peak at zero bias results from supercurrent between the two electrodes (see Supplemental Material [33]). On the contrasting panel, (d) shows the presence of large conductance peaks at voltages marked as $2\Delta^*$ and a strong decrease of conductance within the gap. Unexpectedly, small dips next to the peaks appear marked with the E_d. The figure also marks the values of subgap and normal-state conductance (G_S and G_N) used in further analysis.

$V_{BG} = 15$ V are presented in Figs. 3(c) and 3(d), respectively. For the two segments the conductance behaves differently in the subgap region ($|V_{SD}| < 0.3$ meV). In the absence of the barrier the conductance is enhanced in the subgap regions as expected for the well-transmitting superconductor–normal-metal–superconductor (S-N-S) junction [35]. On the other hand, the segment containing the barrier shows a large suppression at the same bias window due to the low transmission probability for electrons through the InP barrier.

The measurements of the segment without barrier show existence of multiple Andreev reflections (MAR) between the two superconducting contacts indicated by the presence of dips in the subgap conductance [36] at $\pm 2\Delta/e = \pm 400$ μV, $\pm 2\Delta/2e$ marked by arrows in Fig. 3(c), where Δ is the gap of the superconducting electrode. Measurements of another junction displaying also MAR features at $\pm 2\Delta/3e$ are presented in the Supplemental Material [33].

In contrast, the characteristics of the segment with InP barrier is different [see Fig. 3(d)], it has a superconducting gaplike feature: large peaks reminiscent of the superconducting coherence peaks and reduced conductance in between. However, compared to the DOS of metallic superconductors also differences can be seen. (i) The peaks appear at reduced energy marked with $2\Delta^* = \pm 220$ μeV. (ii) At energies above the gap a small dip appears, marked by $E_d = \pm 330$ μeV. (iii) The subgap conductance remains finite even at zero bias voltage. This *softness* of the gap can be characterized by the subgap to normal-state conductance ratio [37], G_S/G_N, which is approximately 0.1 in our case, where $G_S = G(V_{SD} = 0)$ and G_N is the normal-state conductance averaged in a small bias window above the gap [see Fig. 3(d)].

III. DISCUSSION

In the following we concentrate on the analysis of the low-temperature spectroscopy measurements. It is expected that when a superconducting contact is placed on an InAs wire an induced proximity superconducting region appears in the wire in the vicinity of the electrode. Therefore, our structure containing the barrier can be modeled as S-S'-I-S'-S, where I marks the barrier, and S' marks the induced superconducting region in the wire. It is known that in the long junction limit ($L > \xi$, where L is the junction length and ξ is the superconducting coherence length) in S' the superconducting gap becomes reduced as the distance from the SC interface of the superconductor is increased [38]. In our structure this happens on both sides of the barrier. Therefore, our structure to first order can be understood as one proximity-induced superconducting region probes the other. The appropriateness of this picture can be verified with devices, where one of the superconducting electrodes is replaced by the normal one, hence an S-S'-I-N structure is formed. Measurements on such a

structure are given in the Supplemental Material [33] and show similar features, but at smaller energy scale (since only one superconducting electrodes is present), and with reduced energy resolution.

In few channel systems the proximity effect is often explained in the framework of Andreev bound states (ABS) [39,40]. In our geometry, ABSs can be formed between the superconducting electrode and the barrier. The formation of the ABS is shown in Fig. 4(a). An electron traveling in the wire is normal reflected from the barrier, whereas it is Andreev reflected from the superconductor. The same holds for a hole. After two normal and two Andreev reflections, a bound state can be formed. Using the Bohr-Sommerfeld quantization the phase factor acquired by the wave function during the full cycle should be a multiple of 2π:

$$2(k_e - k_h)L - 2\arccos\left(\frac{E}{|\Delta|}\right) = 2\pi n, \qquad (2)$$

where k_e, k_h are the wave numbers of the electron and the hole, L is the distance between the SC electrode and and the barrier, E is the bound-state energy, Δ is the superconducting gap and n is an integer number. In the short-junction limit the first term can be omitted, resulting in $E = \Delta$, however, here this is not the case. $\Delta k = k_e - k_h$ can be approximated from the dispersion relation: $\Delta k = 2E/(\hbar v_F)$, where v_F is the Fermi velocity. Similar equations can be written up for the other side of the barrier. Here for simplicity it is assumed that the energy of the ABS is the same on both sides and within this picture we did not consider bound states connecting the two sides.

In the framework of ABS, the coherence peaks at $V_{SD} = 2\Delta^*/e$ in Fig. 3(d) appear, when the applied bias voltage aligns the occupied ABSs (at energy $-E$) on one side of the barrier with the unoccupied ABS (at $+E$) on the other side of the barrier. Thus the coherence peak position is directly related to the energy of the ABS, i.e., $\Delta^* = E$. Figure 4(b) shows the extracted Δ^* normalized with the bulk gap as a function of the backgate voltage. A small, but steady increase is shown as a function of the gate voltage. Let us estimate now, the trajectory length based on Eq. (2). The control segment without the barrier can be used to extract the electron density and Fermi velocity as a function of backgate voltage. The conductance of the segment without the barrier, which is used for obtaining these parameters is shown on (d) of Fig. 4. This is measured at a dc bias voltage of 1 mV to avoid superconducting features. Using the ABS energy and the Fermi velocity extracted from the reference junction (given in the Supplemental Material [33], with typical values $v_F = 10^6$ m/s) the length of the junction can be extracted using Eq. (2) with $n = 0$. This is shown in Fig. 4(c) as a function of backgate voltage. The extracted trajectory length is 3–4 μm, which is much larger than the nominal length of the InAs segment between the
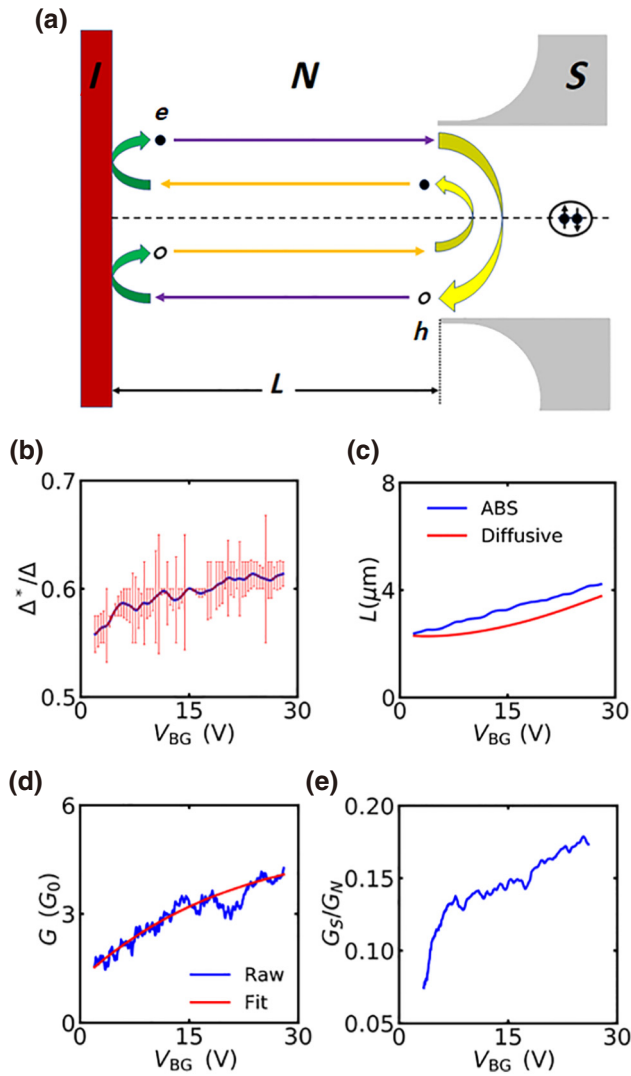
FIG. 4.   Induced superconductivity (a) shows schematics of the formation of Andreev bound states between the superconducting contact and the tunnel barrier. Empty circles represent holes, whereas filled circles represent electronic states. The loop corresponds to the lowest order process to form Andreev bound states. The phases accumulated during the round trip are given by Eq. (2). Panel (b) shows the extracted superconducting gap normalized by the bulk gap of aluminum. For Δ we use 200 μV. Panel (c) shows L_{tr} (in blue) extracted from the Andreev bound-state energy using Eq. (2) as a function of backgate voltage. The red curve shows the path length that an electron travels with diffusion coefficient D from the superconducting contact to the barrier as a function of backgate voltage. Panel (d) shows the normal-state conductance extracted as from Fig. 3(a) at $V_{SD} = 1$ mV. Panel (e) shows the subgap conductance normalized by the normal-state conductance as defined in Fig. 3(e).

barrier and S electrode, which is approximately $L = 150$ nm. The reason for this discrepancy lies in the assumption that our junction is ballistic. Again, we can use the control junction to extract a mean free path (see Supplemental

Material [33]), which is in the order of 20–30 nm. We can also extract the diffusion coefficient, D from the control junction, using Einstein relation and a three-dimensional density of states for the nanowire (shown in the Supplemental Material [33]), which results in values in the range of $D = 0.008$–0.011 m^2/s. With the diffusion constant the effective trajectory length an electron undertakes during its diffusive motion from the SC electrode to the barrier can be calculated: $L_{tr} = (L^2/D)v_F$.

This L_{tr} is plotted in Fig. 4(c) with red and is in quite good agreement with the blue trace extracted from the ABS energy. This good agreement points to the direction that although ABSs give a conceptually simple description of the induced gap, several scattering events take place as an electron propagates from the barrier into the S electrode. This could originate from finite reflection at the S-nanowire interface or from diffusive transport in the nanowire. Note, in our nanowires there are several conductance channels leading to various ABS trajectories, which can be described by a distribution of energies of ABSs. In this case L derived from Δ^* captures the most probable trajectory length. Thus assuming only a single channel and using Eq. (2) is a valid simplification to get an estimate for the typical trajectory length.

In the diffusive theory of superconductivity the Thouless energy $E_{Th} = \hbar D/L^2$, plays the role of the induced gap for long junctions. For junctions in the intermediate regime E_{Th} and Δ determines the induced gap size. Equation (2) can be used to make an estimate on the gap size as a function of E_{Th} and Δ as discussed in the Supplemental Material [33]. Note that the extracted gaps are also in agreement with more complex studies of Ref. [41].

The ABS energy, or with other words the induced gap, shows an increase as a function of the backgate voltage [see Fig. 4(b)]. A similar tendency was observed in Ref. [42], where an increase at low and a clear saturation at larger backgate voltages was seen. In this study they attributed this effect to the transition from long ballistic to the short-junction regime, where the transition was driven by the Fermi velocity change induced by the density change. In our case, the ABS energies are increasing as a function of gate voltage in the full range investigated. The junction is in the transition region between long diffusive and short regime ($L \approx \xi$, see the Supplemental Material [33]), but no clear signatures of this transition is observed. However, a strong increase and saturation behavior is seen for another, S-S'-I-N junction shown in the Supplemental Material, where this behavior might be attributed to the transition from the long diffusive to short-junction regime.

Finally, we comment on the conductance suppression within the gap. The value of subgap conductance normalized by the normal-state conductance is shown in Fig. 4(e) for the entire gate range. This shows an increase as a function of backgate voltage from 0.08 to 0.17. The increase can be understood as a reduction of barrier height as

the electron density increases. These low values are quite promising for future experiments. This subgap suppression is much larger than what was found in Ref. [42] where the barrier was defined by the change of crystallographic structure of the wire and is larger than what one can usually achieve using gate-defined tunnel barriers.

While the values are encouraging for future experiments, for high spectral resolution an even larger subgap conductance suppression would be desirable. It is expected that if the normal-state conductance of the barrier is proportional to $\mathcal{T}$, the transmission value, then the subgap conductance scales with $\mathcal{T}^2$, since two electron charges are transmitted for Andreev-reflection-based transport processes. Therefore, by increasing barrier width (the width of the InP segment), a smaller $\mathcal{T}$, and therefore larger conductance suppression, is expected. Also, since the superconducting contact placed on the wire has finite 150–200 nm extension this results in electrons injected at different distances from the barrier. This results in electron trajectories with different length, and lead also to different ABS energies, hence to a smearing of the gap and reducing subgap conductance suppression. Finally, subgap states present in InAs nanowires discussed in Ref. [43], e.g., stemming from interface inhomegenity can also give contributions to the subgap conductance. However, their role could be better assessed using barriers with smaller transmission.

So far we can describe most of the features in Fig. 3(d) based on Andreev bound states with an effective trajectory length. In Ref. [38] detailed calculations for similar structures have been made based on scattering formalism. These calculations match well with our measurements, even reproducing the dip above the gap (at E_d). This dip usually appears when localized states, resonances are present between the barrier and the superconducting electrodes, in superconductor-insulator-superconductor (*S-I-S*) or *S-I-N* structures [38]. In our case the ABS can play the role of the resonance, which is underlined by the aformentioned detailed theoretical calculation.

IV. CONCLUSIONS

In summary, we show that InP segments embedded in InAs nanowires can be used as tunnel probes for probing SC bound states in the proximitized wire regions. We use thermal-activation measurements to confirm the presence of the InP barriers. Low-temperature transport measurements show an induced gaplike structure, which we describe with the presence of Andreev bound states in the lead segment. We see that the induced gap is gate tunable, originating from the change D (or Thouless energy). The curves showed a subgap conductance suppression below 0.1, which is promising for future applications. Compared to quantum-dot-based probes, or probes based on crystal-phase engineering our InP barrier does not contain internal resonances, therefore will not hybridize with the states to

be probed. These InP segments offer sharp tunnel barriers, where the transmission can be changed by changing the width of the barrier during the growth. We use InP segments with thickness of 5.2 nm, which lead to a subgap suppression of 0.1 (see the Supplemental Material). We estimate the transmission of the barrier is 0.02–0.1. A further increase of the subgap suppression can be achieved by increasing the barrier width. However, in the literature the presence of a soft gap is discussed. This soft gap might also originate from subgap states present in the proximity-induced region, not from the imperfection of the tunnel probe. The presence of such subgap states are important both for qubit or for Majorana devices. With a further increase of the tunnel barrier the presence of these states can be studied. Moreover, it is claimed that using *in situ* grown Al contacts a better controlled proximity region can be achieved, with a reduced number of subgap states [37,44]. Therefore, it is beneficial to combine these *in situ* grown wires with Al shell with the InP tunnel barriers, which would also allow better probing of exotic bound states.

V. METHODS

The InAs/InP nanowire heterostructure of diameter approximately 50 nm with a very narrow InP segment of thickness about $a = 5.2 \pm 0.4$ nm are grown by Au-assisted CBE on InAs(111)B substrates, using trimethylindium (TMIn), tert-butylarsine (TBAs) and tert-butylphosphine (TBP) as metalorganic precursors, with line pressures of 0.2, 0.8, and 4 Torr, respectively [31]. Then nanowires are deposited on a silicon substrate with a 290-nm oxide layer by means of a mechanical manipulator. The device is fabricated by electron-beam lithography (EBL) then Ti/Al layers are deposited with thicknesses of 10/80 nm. Prior to the deposition, the oxide formed on the surface of the InAs is removed with Ar bombardment. For the *S-I-N* structures a separate step *e*-beam step is performed to realize the Ti/Au contacts (10/80 nm). The barriers are located using SEM images, and the growth parameters (distance from gold catalyst).

Low-temperature measurements are done in a Leiden Cryogenics CF-400 top-loading cryo-free dilution refrigerator system with a base temperature of 30 mK. We use a standard lock-in technique at 137 Hz by applying very small ac signal with 10 μV amplitude on the middle contact and measuring the conductance of the two segments via home-built I/V converters as a function of dc bias voltage and backgate voltage.

The data in this publication are available in numerical form online [45].

---

[1] C. M. Lieber and Z. L. Wang, Functional nanowires, MRS Bull. **32,** 99 (2007).

[2] S. Nadj-Perge, S. Frolov, E. Bakkers, and L. P. Kouwenhoven, Spin–orbit qubit in a semiconductor nanowire, Nature **468,** 1084 (2010).

[3] M. Hays, G. de Lange, K. Serniak, D. van Woerkom, D. Bouman, P. Krogstrup, J. Nygård, A. Geresdi, and M. Devoret, Direct Microwave Measurement of Andreev-Bound-State Dynamics in a Semiconductor-Nanowire Josephson Junction, Phys. Rev. Lett. **121,** 047001 (2018).

[4] L. Tosi, C. Metzger, M. Goffman, C. Urbina, H. Pothier, S. Park, A. L. Yeyati, J. Nygård, and P. Krogstrup, Spin-Orbit Splitting of Andreev States Revealed by Microwave Spectroscopy, Phys. Rev. X **9,** 011010 (2019).

[5] L. Hofstetter, S. Csonka, J. Nygård, and C. Schönenberger, Cooper pair splitter realized in a two-quantum-dot *y*-junction, Nature **461,** 960 (2009).

[6] A. Das, Y. Ronen, M. Heiblum, D. Mahalu, A. V. Kretinin, and H. Shtrikman, High-efficiency Cooper pair splitting demonstrated by two-particle conductance resonance and positive noise cross-correlation, Nat. Commun. **3,** 1165 (2012).

[7] G. Fülöp, F. Domínguez, S. d'Hollosy, A. Baumgartner, P. Makk, M. H. Madsen, V. Guzenko, J. Nygård, C. Schönenberger, A. L. Yeyati, and S. Csonka, Magnetic Field Tuning and Quantum Interference in a Cooper Pair Splitter, Phys. Rev. Lett. **115,** 227003 (2015).

[8] G. Fülöp, S. d'Hollosy, A. Baumgartner, P. Makk, V. Guzenko, M. Madsen, J. Nygård, C. Schönenberger, and S. Csonka, Local electrical tuning of the nonlocal signals in a Cooper pair splitter, Phys. Rev. B **90,** 235412 (2014).

[9] V. Mourik, K. Zuo, S. M. Frolov, S. Plissard, E. P. Bakkers, and L. P. Kouwenhoven, Signatures of Majorana fermions in hybrid superconductor-semiconductor nanowire devices, Science **336,** 1003 (2012).

[10] M. Deng, S. Vaitiekėnas, E. B. Hansen, J. Danon, M. Leijnse, K. Flensberg, J. Nygård, P. Krogstrup, and C. M. Marcus, Majorana bound state in a coupled quantum-dot hybrid-nanowire system, Science **354,** 1557 (2016).

[11] H. Zhang, C.-X. Liu, S. Gazibegovic, D. Xu, J. A. Logan, G. Wang, N. Van Loo, J. D. Bommer, M. W. De Moor, D.

Car, *et al.*, Quantized Majorana conductance, Nature **556,** 74 (2018).

[12] R. Lutchyn, E. Bakkers, L. P. Kouwenhoven, P. Krogstrup, C. Marcus, and Y. Oreg, Majorana zero modes in superconductor–semiconductor heterostructures, Nat. Rev. Mater. **3,** 52 (2018).

[13] E. J. Lee, X. Jiang, M. Houzet, R. Aguado, C. M. Lieber, and S. De Franceschi, Spin-resolved andreev levels and parity crossings in hybrid superconductor–semiconductor nanostructures, Nat. Nanotechnol. **9,** 79 (2014).

[14] T. Sand-Jespersen, J. Paaske, B. M. Andersen, K. Grove-Rasmussen, H. I. Jørgensen, M. Aagesen, C. Sørensen, P. E. Lindelof, K. Flensberg, and J. Nygård, Kondo-Enhanced Andreev Tunneling in InAs Nanowire Quantum Dots, Phys. Rev. Lett. **99,** 126603 (2007).

[15] A. Jellinggaard, K. Grove-Rasmussen, M. H. Madsen, and J. Nygård, Tuning Yu-Shiba-Rusinov states in a quantum dot, Phys. Rev. B **94,** 064520 (2016).

[16] K. Grove-Rasmussen, G. Steffensen, A. Jellinggaard, M. H. Madsen, R. Žitko, J. Paaske, and J. Nygård, Yu–Shiba–Rusinov screening of spins in double quantum dots, Nat. Commun. **9,** 2376 (2018).

[17] Z. Scherübl, G. Fülöp, C. P. Moca, J. Gramich, A. Baumgartner, P. Makk, T. Elalaily, C. Schönenberger, J. Nygård, G. Zaránd, and S. Csonka, Large spatial extension of the zero-energy Yu-Shiba-Rusinov state in magnetic field, arXiv:1906.08531 (2019).

[18] W. Chang, V. Manucharyan, T. S. Jespersen, J. Nygård, and C. M. Marcus, Tunneling Spectroscopy of Quasiparticle Bound States in a Spinful Josephson Junction, Phys. Rev. Lett. **110,** 217005 (2013).

[19] C. Fasth, A. Fuhrer, M. T. Björk, and L. Samuelson, Tunable double quantum dots in InAs nanowires defined by local gate electrodes, Nano Lett. **5,** 1487 (2005).

[20] A. Pfund, I. Shorubalko, K. Ensslin, and R. Leturcq, Suppression of Spin Relaxation in an InAs Nanowire Double Quantum Dot, Phys. Rev. Lett. **99,** 036801 (2007).

[21] V. Zannier, F. Rossi, V. G. Dubrovskii, D. Ercolani, S. Battiato, and L. Sorba, Nanoparticle stability in axial InAs–InP nanowire heterostructures with atomically sharp interfaces, Nano. Lett. **18,** 167 (2018).

[22] L. Samuelson, C. Thelander, M. T. Björk, M. Borgstrm, K. Deppert, K. A. Dick, A. E. Hansen, T. Mårtensson, N. Panev, A. I. Persson, W. Seifert, N. Sköld, M. W. Larsson, and L. R. Wallenberg, Semiconductor nanowires for 0D and 1D physics and applications, Physica E: Low-Dimen. Syst. Nanostruct. **25,** 313 (2004).

[23] F. S. Thomas, A. Baumgartner, L. Gubser, C. Jünger, G. Fülöp, M. Nilsson, F. Rossi, V. Zannier, L. Sorba, and C. Schönenberger, Highly symmetric and tunable tunnel couplings in InAs/InP nanowire heterostructure quantum dots, arXiv:1909.07751 (2019).

[24] S. Roddaro, A. Pescaglini, D. Ercolani, L. Sorba, and F. Beltram, Manipulation of electron orbitals in hard-wall InAs/InP nanowire quantum dots, Nano Lett. **11,** 1695 (2011).

[25] F. Rossella, A. Bertoni, D. Ercolani, M. Rontani, L. Sorba, F. Beltram, and S. Roddaro, Nanoscale spin rectifiers controlled by the Stark effect, Nat. Nanotechnol. **9,** 997 (2014).

[26] L. Romeo, S. Roddaro, A. Pitanti, D. Ercolani, L. Sorba, and F. Beltram, Electrostatic spin control in InAs/InP nanowire quantum dots, Nano Lett. **12,** 4490 (2012).

[27] A. Fuhrer, L. E. Fröberg, J. N. Pedersen, M. W. Larsson, A. Wacker, M.-E. Pistol, and L. Samuelson, Few electron double quantum dots in InAs/InP nanowire heterostructures, Nano. Lett. **7,** 243 (2007).

[28] A. C. Bleszynski-Jayich, L. E. Fröberg, M. T. Björk, H. Trodahl, L. Samuelson, and R. Westervelt, Imaging a one-electron InAs quantum dot in an InAs/InP nanowire, Phys. Rev. B **77,** 245327 (2008).

[29] M. Josefsson, A. Svilans, A. M. Burke, E. A. Hoffmann, S. Fahlvik, C. Thelander, M. Leijnse, and H. Linke, A quantum-dot heat engine operating close to the thermodynamic efficiency limits, Nat. Nanotechnol. **13,** 920 (2018).

[30] M. Björk, B. Ohlsson, T. Sass, A. Persson, C. Thelander, M. Magnusson, K. Deppert, L. Wallenberg, and L. Samuelson, One-dimensional heterostructures in semiconductor nanowhiskers, Appl. Phys. Lett. **80,** 1058 (2002).

[31] V. Zannier, F. Rossi, D. Ercolani, and L. Sorba, Growth dynamics of InAs/InP nanowire heterostructures by Au-assisted chemical beam epitaxy, Nanotechnology **30,** 094003 (2019).

[32] M. T. Björk, B. J. Ohlsson, T. Sass, A. I. Persson, C. Thelander, M. H. Magnusson, K. Deppert, L. R. Wallenberg, and L. Samuelson, One-dimensional steeplechase for electrons realized, Nano Lett. **2,** 87 (2002).

[33] See Supplemental Material at http://link.aps.org/supplemental/10.1103/PhysRevApplied.14.044002 for further information about comparison of transport properties of wires with and without barriers at low temperature, MAR and supercurrent measurements for the reference segment, measurements on normal-metal–insulator–superconductor (*N*-*I*-*S*) structures, density, and Fermi velocity calculation for the reference segment (following Refs. [46,47]) and comparison between the calculated Thouless energy and measured gap size.

[34] G. Nylund, K. Storm, S. Lehmann, F. Capasso, and L. Samuelson, Designed quasi-1D potential structures realized in compositionally graded $InAs_{1-x}P_x$ nanowires, Nano. Lett. **16,** 1017 (2016).

[35] T. S. Jespersen, M. Polianski, C. Sørensen, K. Flensberg, and J. Nygård, Mesoscopic conductance fluctuations in InAs nanowire-based SNS junctions, New J. Phys. **11,** 113025 (2009).

[36] H. Gunel, N. Borgwardt, I. Batov, H. Hardtdegen, K. Sladek, G. Panaitov, D. Grutzmacher, and T. Schapers, Crossover from Josephson effect to single interface Andreev reflection in asymmetric superconductor/nanowire junctions, Nano Lett. **14,** 4977 (2014).

[37] W. Chang, S. Albrecht, T. Jespersen, F. Kuemmeth, P. Krogstrup, J. Nygård, and C. M. Marcus, Hard gap in epitaxial semiconductor–superconductor nanowires, Nat. Nanotechnol. **10,** 232 (2015).

[38] E. Zhitlukhina, I. Devyatov, O. Egorov, M. Belogolovskii, and P. Seidel, Anomalous inner-gap structure in transport characteristics of superconducting junctions with degraded interfaces, Nanoscale Res. Lett. **11,** 58 (2016).

[39] B. Pannetier and H. Courtois, Andreev reflection and proximity effect, J. Low Temp. Phys. **118,** 599 (2000).

[40] T. M. Klapwijk, Proximity effect from an Andreev perspective, J. Supercond. **17,** 593 (2004).

[41] J. Hammer, J. C. Cuevas, F. Bergeret, and W. Belzig, Density of states and supercurrent in diffusive SNS junctions: Roles of nonideal interfaces and spin-flip scattering, Phys. Rev. B **76,** 064514 (2007).

[42] C. Jünger, A. Baumgartner, R. Delagrange, D. Chevallier, S. Lehmann, M. Nilsson, K. A. Dick, C. Thelander, and C. Schönenberger, Spectroscopy of the superconducting proximity effect in nanowires using integrated quantum dots, Commun. Phys. **2,** 76 (2019).

[43] S. Takei, B. M. Fregoso, H.-Y. Hui, A. M. Lobos, and S. Das Sarma, Soft Superconducting Gap in Semiconductor Majorana Nanowires, Phys. Rev. Lett. **110,** 186803 (2013).

[44] P. Krogstrup, N. L. B. Ziino, W. Chang, S. M. Albrecht, M. H. Madsen, E. Johnson, J. Nygård, C. Marcus, and T. S. Jespersen, Epitaxy of semiconductor-superconductor nanowires, Nat. Mater. **14,** 400 (2015).

[45] T. Elalaily, O. Kurtossy, V. Zannier, Z. Scherubl, I. E. Lukacs, P. Srivastava, F. Rossi, L. Sorba, S. Csonka, and P. Makk, Data for: Probing Proximity-Induced Superconductivity in an InAs Nanowire Using Built-In Barriers, (2020) https://doi.org/10.5281/zenodo.3519430.

[46] M. D. Schroer and J. R. Petta, Correlating the nanostructure and electronic properties of InAs nanowires, Nano Lett. **10,** 1618 (2010).

[47] O. Wunnicke, Gate capacitance of back-gated nanowire field-effect transistors, Appl. Phys. Lett. **89,** 083102 (2006).